11

SANDIA REPORT

SAND2012-8027
Unlimited Release
Printed September 2012

Probing Surface & Transport Phenomena in Energy Materials Under Operating Conditions

William C. Chueh, Farid El Gabaly, Anthony H. McDaniel, Kevin F. McCarty

Prepared by
Sandia National Laboratories
Albuquerque, New Mexico 87185 and Livermore, California 94550

Sandia National Laboratories is a multi-program laboratory managed and operated by Sandia Corporation, a wholly owned subsidiary of Lockheed Martin Corporation, for the U.S. Department of Energy's National Nuclear Security Administration under contract DE-AC04-94AL85000.

Issued by Sandia National Laboratories, operated for the United States Department of Energy by Sandia Corporation.

Available to DOE and DOE contractors from
U.S. Department of Energy
Office of Scientific and Technical Information
P.O. Box 62
Oak Ridge, TN 37831

Telephone: (865) 576-8401
Facsimile: (865) 576-5728
E-Mail: reports@adonis.osti.gov
Online ordering: http://www.osti.gov/bridge

Available to the public from
U.S. Department of Commerce
National Technical Information Service
5285 Port Royal Rd.
Springfield, VA 22161

Telephone: (800) 553-6847
Facsimile: (703) 605-6900
E-Mail: orders@ntis.fedworld.gov
Online order: http://www.ntis.gov/help/ordermethods.asp?loc=7-4-0#online

SAND2012-8027
Unlimited Release
Printed September 2012

In-situ Probing Surface & Transport Phenomena in Energy Materials

William C. Chueh, Farid El Gabaly, Kevin F. McCarty
Materials Physics Department
Sandia National Laboratories
7011 East Ave.
Livermore, California 87185-MS9161

Anthony H. McDaniel
Combustion Research Facility
Sandia National Laboratories
7011 East Ave.
Livermore, California 87185-MS9161

Abstract

Efficient conversion of energy between sunlight, chemical bonds, and electricity is crucial towards a closed-loop energy cycle. We have applied synchrotron-based X-ray spectroscopy and microscopy techniques to investigate the conversion of electricity to and from chemical bonds in fuel cells, electrolyzers, and intercalation batteries. Using these techniques, we have tracked the motions from electrons, oxygen ions, and lithium ions at interfaces and in the bulk of electrochemically-active materials. New insights in gas-solid surface electrochemistry, and solid-solid phase transformation are guiding the development of better materials for a wide range of energy conversion and storage devices.

ACKNOWLEDGMENTS

The authors gratefully acknowledge Josh Sugar, Norm Bartelt, Josh Whaley, and Mark Homer at Sandia Livermore for their contribution to this project. The authors also acknowledge Hendrik Bluhm, Tolek Tyliszczak, Zhi Liu, Michael Grass, Andrey Shavorskiy, and David Kilcoyne from Lawrence Berkeley National Laboratory for their assistance with experiments at the Advance Light Source.

Portion of this report is reproduced from the following publications:

W. C. Chueh, A. H. McDaniel, M. E. Grass, Y. Hao, N. Jaibeen, Z. Liu, S. M. Haile, K. F. McCarty, H. Bluhm, F. El Gabaly. High Stability and Reactivity of Ce^{3+} on Doped CeO_2 Surface Revealed In operando. *Chem. Mater.* **24**, 1876-1882 (2012).

W. C. Chueh, F. El Gabaly, J. D. Sugar, N. C. Bartelt, K. R. Fenton, K. R. Zavadil, T. Tyliszczak, W. Lai, K. F. McCarty. Intercalation Pathway in Many-Particle $LiFePO_4$ Electrode Revealed by Nanoscale State-of-Charge Mapping. *Submitted.*

CONTENTS

FIGURES

TABLES

1. INTRODUCTION

In one hour, more energy from sunlight strikes the Earth than the amount consumed by the entire planet in one year.[1] As the most abundant energy source, the sun must play a large role in any global-scale renewable energy conversion strategy. However, tapping into this vast resource does not come without challenges. The intermittent and geographically varying nature of solar radiation means that storage and delivery, of solar-derived energy are critical steps required for mass utilization. Chemical bonds are one of the most effective mediums for storing energy because of their high energy densities, both as bonds in fuels such as hydrogen, and as chemical bonds in intercalation compounds such as lithium-ion battery electrodes.

In this report, we will discuss the application of synchrotron-based spectroscopy and microscopy techniques to understand materials phenomena relevant to the conversion of electricity to and from chemical bonds. The first part of this report focuses on in-situ study of elevated-temperature electro-catalyst for hydrogen oxidation and water-splitting. The second part of this report focuses on phase transformation in lithium-ion battery electrodes.

2. IN-SITU STUDY OF CERIA-BASED ELECTROCATALYSTS

2.1 Introduction

Mixed-valent cerium-based oxides (ceria) are among the most investigated compounds in heterogeneous chemical[2] and electrochemical catalysis.[3-6] In chemical catalysis, ceria is typically used as an active support. The ceria/catalyst interface is known to catalyze surface reactions,[7,8] whereas the bulk serves as an oxygen reservoir. In electro-catalysis, on the other hand, mixed ionic and electronic conductivity (with electrons localized around Ce[9,10]) is essential for rendering ceria an excellent non-metallic electrode in solid oxide fuel cells and electrolyzers.[11-14] At the same time, the surface characteristics result in remarkable electro-catalytic activity, even in the absence of any metal co-catalyst.[15]

Understanding the behavior of surface reactive species is crucial towards establishing the reaction mechanism. Ce^{3+} and oxygen vacancies are thought to be the active sites on ceria surfaces[16-18] in reactions such as hydrolysis: $(H_2O_{(g)} + Ce^{3+} \rightarrow H_{2(g)} + O^{2-} + Ce^{4+})$, with the surface undergoing a Ce^{3+}/ Ce^{4+} redox cycle during the complete catalytic reaction.[2] Several studies have shown that the surface concentrations of these active species can be higher than the bulk, potentially explaining ceria's high chemical activity[16-19] However, the behavior of these active surface species is not well-understood, in part because studies involving mixed-valent materials are complicated by the fact that both the bulk and the surface participate in the catalytic reactions.

Establishing the relationship between surface and bulk oxidation states has been impeded by a variety of experimental difficulties in measuring the surface and the bulk states at the same time under catalytically-relevant conditions. The majority of the experimental studies so far have been carried out using *ex situ* techniques (such as X-ray photoelectron spectroscopy, XPS)[20-26] or non-equilibrium techniques[27] (such as temperature-programmed reduction). In the former, the surface state under catalytic conditions cannot be preserved by quenching due to the high mobilities of Ce^{3+} and oxygen vacancies; in the latter, kinetic and thermodynamic contributions to non-equilibrium experiments are difficult to separate.[27] In theory, bulk equilibrium techniques (*e.g.*, thermogravimetry,[28] calorimetry,[29] and titration[30]) can be made surface sensitive by using samples with high (and variable) surface area. However, the surface area was shown to be unstable during the course of the experiment[30]. Some *in situ* studies have emerged recently,[13,19,31] though none have successfully achieved the desired surface *and* bulk sensitivities.

The accepted view on the behavior of reactive Ce^{3+} species, mostly based on theoretical calculations[17,18,32-39], is that the segregation of Ce^{3+} species to the surface is driven by a change in the oxidation enthalpy. Furthermore, in analyzing kinetics of electrochemical reactions, the concentration of the surface species is often assumed to have the same dependence on the environment as the bulk species.[40,41]

2.2 Experimental Methods

2.2.1 Sample Preparation

Thin-film Pt electrical contacts (~ 100 nm thick) were applied on both sides of a $Y_{0.16}Zr_{0.84}O_{1.92}$ (YSZ) (100) single crystal (MTI Corp.) and patterned via metal-liftoff

photolithography. The metal pattern consists of line patterns 20 μm in width and spaced 140 μm apart. After annealing the patterned substrate at 700 °C in air to stabilize the metal microstructure, ~ 1 μm thick $Sm_{0.2}Ce_{0.8}O_{1.9}$ (SDC) thin films were deposited on both sides of the crystal by pulsed-laser deposition (PLD, Neocera, with Coherent 102 KrF 248 nm excimer laser, ~ 2 J cm^{-2}, 20 Hz). The PLD target was compacted from 99.99 % purity powder (Nextech Materials) and sintered at 1,250 °C for 5 h in an alumina tube dedicated to the processing of SDC. The deposition was carried out at ~ 650 °C under 20 millitorr O_2. After the film was deposited on the second side, the sample was annealed at ~ 650 °C for 1 h in the PLD chamber under 100 Torr O_2.

2.2.2 Structural & Chemical Analysis

Bulk crystallinity was characterized by X-ray diffractometry (Panalytical MRD). Microstructure was examined using a Carl Zeiss LEO 1550VP scanning electron microscope as well as using a FEI Tecnai F30 transmission electron microscope. A JEOL JXA-8200 electron probe microanalyzer was employed for bulk chemical analysis, with $CePO_4$ and $SmPO_4$ serving as the standards. Surface crystallinity was examined *in situ* using an Elmitec LEEM III low-energy electron microscope at temperatures between 600 and 740 °C and at pressures between 10^{-6} and 10^{-7} Torr in O_2 or H_2.

2.2.3 Electrochemical Ambient-Pressure X-ray Photoelectron Spectroscopy

Ambient pressure XPS measurements were carried out at the Advanced Light Source at Lawrence Berkeley National Laboratory, beamline 11.0.2, equipped with a Specs Phoibos 150 ambient pressure electron spectrometer.[42] Select experiments were also performed at beamline 9.3.2, equipped with a Scienta R4000 HiPP spectrometer.[43] High surface sensitivity was achieved by using a low photoelectron kinetic energy (270 eV) (effective electron attenuation length of ~ 4 Å after accounting for electron emission angle, unless otherwise noted). Data were collected over the photon energy range between 270 and 1150 eV and binding energy was calibrated using the Pt $4f_{7/2}$ peak. The resulting spectra were quantified using two independent methods based on (1) valence band (localized Ce 4*f*)[22,24,25,36,44] and (2) core level (Ce 3*d*)[44-47] photoelectron spectra. The surface Sm dopant concentration was also investigated.

At both beamlines, temperature control and electrical contact to the cell were achieved using a custom-designed electrochemical platin with a ceramic heater and Au/Pd coated W probes.[48] A wound Pt wire was placed between the heater and the sample to make backside electrical and thermal connection; probes contacted the topside of the sample under X-ray analysis. Catalytic effects from low-surface area metal contacts are expected to be small, as recently shown by the authors.[15] Gas-phase oxygen activity was controlled by introduction of ultra high purity H_2, O_2, and/or H_2O to the analyzer chamber via leak valves, with the chamber actively pumped through the entrance aperture of the electron analyzer.

Zero-bias electrochemical impedance spectroscopy was performed using a Gamry PCI4-750 or a Bio-Logic SP-300, with the perturbation voltage limited to 10 mV to avoid broadening of photoelectron peaks. Sample temperature was determined from the substrate (YSZ) ionic conductivity. For calibration, the ionic conductivity of the cell was measured separately inside the blackbody environment of an electric furnace. The bulk Ce oxidation state was quantified precisely using capacitance values, also determined by impedance spectroscopy. Chemical

capacitance in ceria arises from the change in oxygen content in response to an externally-applied electrochemical perturbation[49,50] and provides sensitivity to bulk Ce^{3+} fraction ($[Ce^{3+}]_{bulk}$) as low as 10^{-3}.[49]

2.3 Results & Discussions

2.3.1 Structural & Surface Characterizations

The sample consists of two morphological regions: polycrystalline SDC grown over the buried Pt metal patterns covering 13 % of the analysis region, and epitaxial SDC grown over the YSZ single crystal substrate in the remaining region. The surface crystal structure of the sample after ambient pressure XPS analysis was characterized *in situ* using low-energy electron diffraction (LEED) at high temperatures. Specifically, the surface was examined under both oxidizing condition (1.8×10^{-6} Torr O_2, 740 °C) and under reducing condition (1.0×10^{-7} Torr H_2, 600 °C). Although the total pressure here was many orders of magnitude lower than that in the ambient pressure XPS experiment, the two extreme oxygen partial pressures bracket all of the conditions in the ambient pressure experiment. In the region of SDC grown epitaxially, a weak but sharp LEED pattern was observed, shown in Figure 1. The spot separation is consistent with first-order diffraction from a SDC(100) surface. Somewhat surprisingly, the oxidizing and reducing conditions gave the same diffraction pattern, at least over the limited energy range for which there was appreciable diffraction intensity. The polycrystalline regions grown over the buried Pt patterns gave no LEED pattern, probably due to the large surface roughness. These results show that the majority (> 80 %) of the ceria surface consists of well-defined (100)-type facets.

Si was the only impurity detected in the XPS survey scans and there was no evidence of X-ray induced damage or reduction.

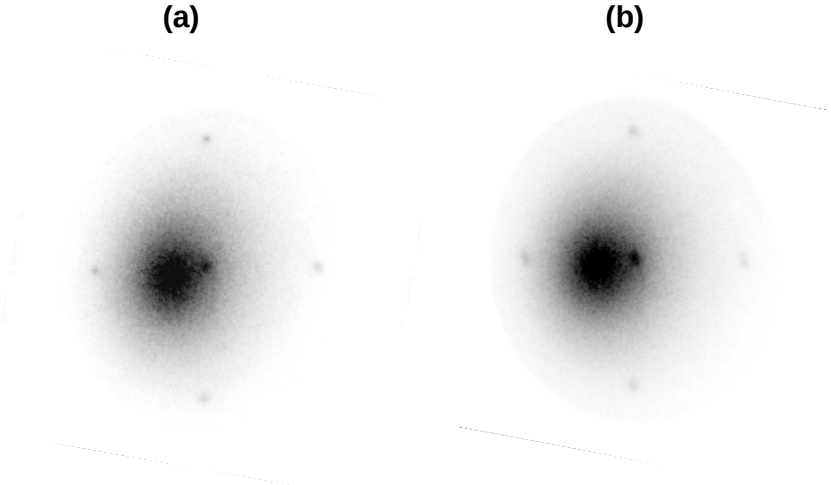

Figure 1. *In-situ* low-energy electron diffraction patterns for SDC collected at **(a)** 1.8×10^{-6} Torr O_2 , 740 °C (oxidizing condition) and **(b)** 1.0×10^{-7} Torr H_2, 600 °C (reducing condition) using 19 eV electrons. The patterns are consistent with a first-order diffraction from SDC(100). These diffuse features are due to secondary electrons.

2.3.2 Bulk & Surface Oxidation States

The bulk Ce oxidation state changes systematically in response to changes in oxygen partial pressure and temperature in the XPS chamber, as shown in Figure 2. The $[Ce^{3+}]_{bulk}$ exhibits a $p_{O_2}^{-1/4}$ dependence, characteristic of acceptor-doped ceria in the dilute solution regime.[11] The magnitude of $[Ce^{3+}]_{bulk}$ agrees very well with literature values, the grey line in Figure 2, and confirms that bulk thermodynamic equilibrium has been achieved. In the temperature-pressure range examined, $[Ce^{3+}]_{bulk}$ varied by a factor of 30, from 1.3 to 40 × 10^{-3} (from $Sm_{0.2}Ce_{0.8}O_{1.899}$ to $Sm_{0.2}Ce_{0.8}O_{1.880}$).

Typical *in operando* Ce 4*f* and Ce 3*d* X-ray photoelectron spectra (of the type used to generate the $[Ce^{3+}]_{surf}$ data in Figure 2) are shown in Figure 3, where the corresponding bulk Ce oxidation states are labeled. In the valence band spectra, the presence of Ce^{3+} species is indicated by the occupied Ce 4*f* gap state at ~ 2 eV binding energy. In the Ce 3*d* core-level spectra, final state effects lead to peak splitting, with select peaks (marked in Figure 3b) attributed to the Ce^{3+} state. Reference spectra collected under highly oxidizing condition (465 °C and 7 × 10^{-6} Torr O_2) are also shown. Even in the absence of any quantitative analysis, it is apparent that the spectral feature changed significantly from $[Ce^{3+}]_{bulk}$ = 0 (fully oxidized $Sm_{0.2}Ce_{0.8}O_{1.900}$) to 1.3 × 10^{-3} ($Sm_{0.2}Ce_{0.8}O_{1.899}$) but *much less so* during the much larger change in the bulk oxidation state from 1.3 × 10^{-3} to 40 × 10^{-3} ($Sm_{0.2}Ce_{0.8}O_{1.880}$). The Ce 4*f* and Ce 3*d* photoelectron were analyzed

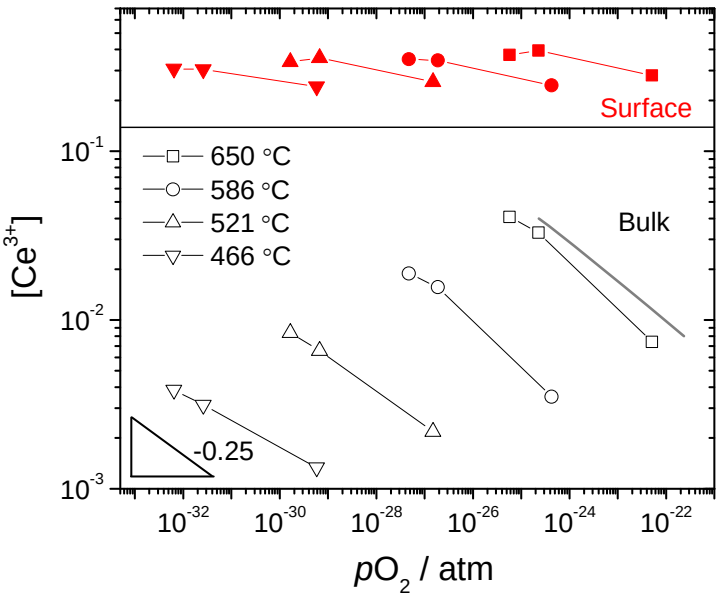

Figure 2: (left) Equilibrium fraction of surface Ce^{3+} (closed) and bulk Ce^{3+} (open) measured at various H_2-H_2O-O_2 atmospheres and temperatures. Value of 1 indicates that Ce is entirely in the reduced 3+ oxidation state. Lines are for guiding the eyes. Grey line (650 °C) is extrapolated from the thermogravimetric measurement of bulk $Sm_{0.2}Ce_{0.8}O_{1.9-\delta}$ from reference 60. Electron effective attenuation length (accounting for the electron emission angle) is 4 Å for these measurements.

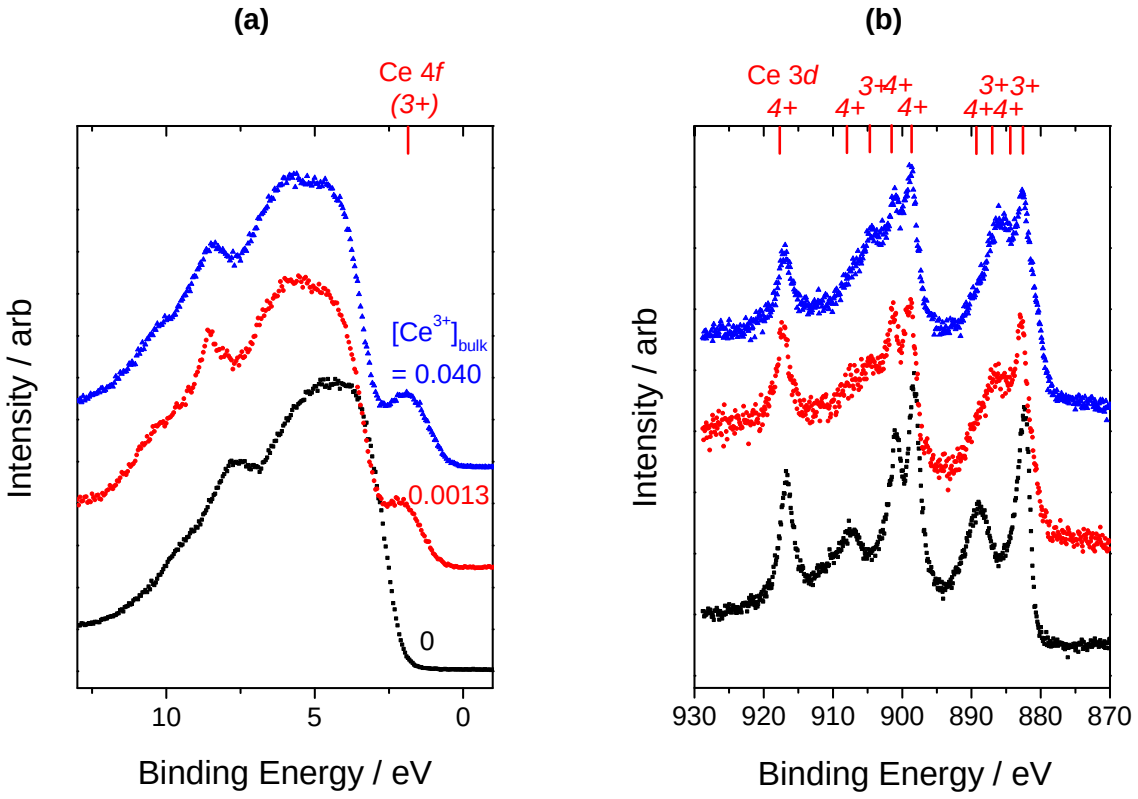

Figure 3. Typical SDC **(a)** valence band and **(b)** Ce 3d core level X-ray photoelectron spectra at various bulk oxidation states measured in operando. Partially reduced SDC was measured at 650 °C ($[Ce^{3+}]_{bulk}$ = 0.040) and 466 °C ($[Ce^{3+}]_{bulk}$ = 0.0013) and oxidized SDC ($[Ce^{3+}]_{bulk}$ = 0) at 466 °C. Spectral features assigned to Ce^{3+} and Ce^{4+} oxidation states are shown. Slight shift in the oxidized SDC spectra relative to the reduced spectra is due to change in the Fermi level upon oxidation.

independently to determine surface Ce^{3+} fraction ($[Ce^{3+}]_{surf}$). A good consistency was obtained, confirming the robustness of the quantification methodology. Since quantification based on the Ce 4*f* peaks gave slightly less scatter, we report these values in Figure 2.

The most striking feature of the oxidation behavior revealed in Figure 2 are the dramatic differences in the equilibrium oxidation states of Ce in the surface and bulk regions. Under all conditions examined, the surface $[Ce^{3+}]$ values are much greater than those of the bulk, indicating that the surface is substantially more reduced. The ratio of surface to bulk $[Ce^{3+}]$ (Figure 4) ranges from ~ 10 to ~180, with the differences largest at lower temperatures and higher oxygen activities, *i.e.*, under more oxidizing conditions. Beyond the differences in absolute magnitude of $[Ce^{3+}]$ in the bulk and surface, the temperature and oxygen activity dependences differ starkly. In contrast to the bulk, the surface Ce^{3+} concentration depends only weakly on these parameters (Figure 2). Specifically, under the temperature-pressure conditions probed, $[Ce^{3+}]_{surf}$ only changed by a factor 1.6, whereas $[Ce^{3+}]_{bulk}$ changed by a factor of 30. Similarly, $\left(\partial \log[Ce^{3+}]/\partial \log p_{O_2}\right)_T$ (the slope in Figure 2), is much weaker for the surface than for the bulk, with average values of -0.05 and -0.21, for the respective regions. This observation has

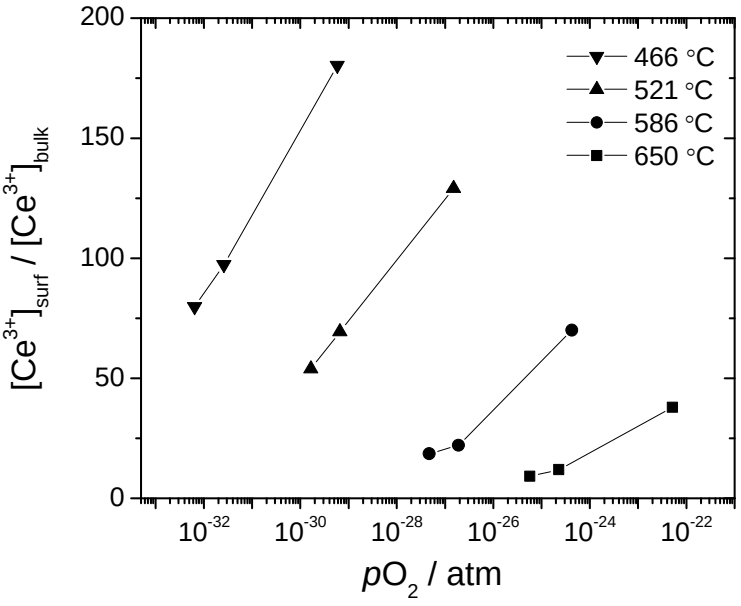

Figure 4. Ratio of the surface to bulk Ce^{3+} concentration. Lines are for guiding the eyes.

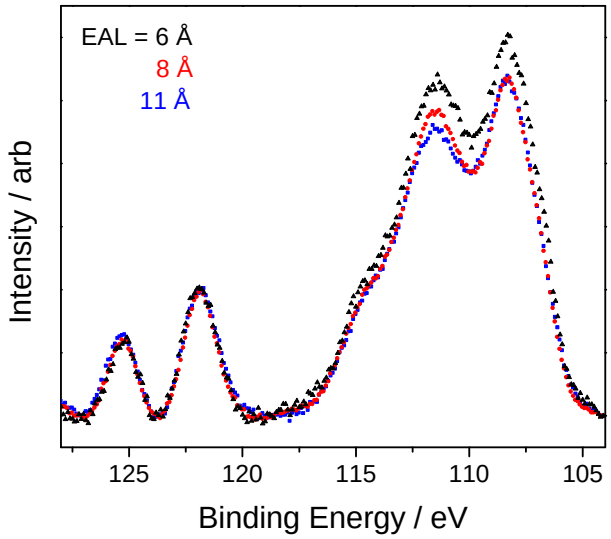

Figure 5. Depth-resolved Ce 4d photoelectron spectra obtained by varying the incident photon energy ($h\upsilon$ = 350, 490, and 750 eV). T = 650 °C, $p_{O_2} = 10^{-25}$ atm, $p_{H_2} = 0.16$ Torr, $p_{H_2O} = 0.16$ Torr.

significant implications for interpreting the catalytic activity of ceria-based systems, as discussed below.

The direct determination of oxygen vacancy concentration and surface charge is beyond the scope of this work. Hence, while the data clearly demonstrate that the surface is strongly reduced relative to the bulk with a substantially higher Ce^{3+} concentration, it is not known whether the

excess electrons in the surface region are charge-balanced by an equivalent number of oxygen vacancies (or other positively charged defects). As commonly observed in ceria internal grain boundaries[51,52], the interfacial region carries a positive charge and induces the formation of a negatively-charged space-charge layer to screen the bulk from the interfacial charge, with the spatial extent of the layer determined in part by the Debye screening length.[53] Such a diffuse double-layer may also be present adjacent to the surface in this work. In heavily doped materials such as SDC, the Debye length can be in the sub-nm range, and therefore needs to be considered.

In both the surface and the space-charge regions, the Ce^{3+} concentration would differ from the bulk values. Using depth-resolved XPS, we assess whether the observed Ce^{3+} enrichment in the near-surface region originates from the surface region or from the diffuse space-charge layer. Within the space-charge region, an electrostatic field is present at equilibrium, and shifts the kinetic energy of photoelectrons.[54] However, Ce 4*d* spectra collected at various attenuation lengths from 6 to 11 Å display no energy shift from one another, within the photon energy resolution (Figure 5). Given the expected space-charge thickness in SDC, this observation suggests that the enriched Ce^{3+} is located on the surface rather than in the adjacent space-charge region.

2.3.3 Effect of Adsorbates on Surface Oxidation State

Given the relatively high H_2 and H_2O pressures employed in this work and the high surface concentrations of surface reactive species observed, one can speculate that H_2 and H_2O may interact directly with the surface via adsorbates.[55] To deconvolute possible adsorbate effects from oxygen activity effects, the chemical potentials of hydrogen and water vapor were varied

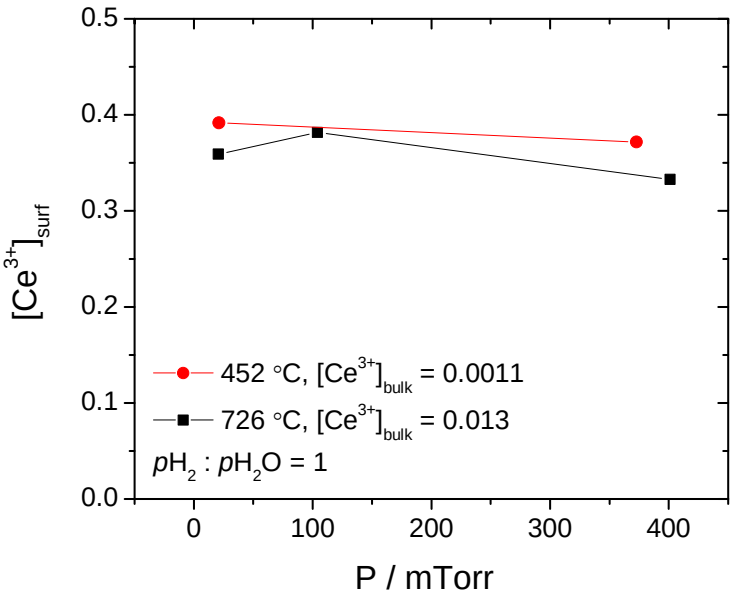

Figure 6. The effect of adsorbates on the extent of surface Ce reduction, examined by varying the total gas pressure while maintaining the same oxygen activity (i.e., holding $p_{H_2} : p_{H_2O}$ constant). Electrochemical impedance spectra taken simultaneously confirmed that the bulk oxidation state is independent of total pressure for each temperature. Electron effective attenuation length (accounting for the electron emission angle) is 6 Å for these measurements. Lines are for guiding the eyes.

while maintaining the oxygen activity. This was achieved by changing the total gas pressure of the system while maintaining a constant $p_{H_2} : p_{H_2O}$ ratio. As a consequence of the equilibrium relationship, $p_{O_2} = \frac{\left(p_{H_2O}\right)^2}{K(T)\left(p_{H_2}\right)^2}$, such conditions imply a constant oxygen activity for a given temperature. H_2 and H_2O are assumed not to interact with bulk ceria directly at the relatively high temperature examined, which has been shown experimentally.[56] Thus, changing the total gas pressure of the system while maintaining a constant $p_{H_2} : p_{H_2O}$ ratio at a constant temperature gives the same oxygen activity, and hence the same bulk oxidation state. Here, $p_{H_2} : p_{H_2O}$ was fixed at 1 and the total pressure varied from ~ 20 to 400 millitorr.

The impedance spectroscopy revealed that the bulk oxidation state was essentially unchanged, confirming the constant oxygen activity. Similarly, despite increasing the total pressure by a factor of 20, $[Ce^{3+}]_{surf}$ varied negligibly (Figure 6), ranging between 0.33 and 0.38 at 650 °C and between 0.37 and 0.39 at 450 °C. This observation confirms that change in the chemical potential of H_2 and H_2O do not affect the oxidation state of the surface, at least under the conditions probed, and suggests that analyzing the oxidation states using oxygen partial pressure as the sole gas-phase potential is appropriate. Furthermore, the results imply that adsorbates are not strongly coupled to the surface Ce oxidation state. This is consistent with our observation that surface hydroxyl concentration is negligible at 650 °C.

2.3.4 Chemical Potential of Surface & Bulk Oxygen

Having established that variation in the oxygen partial pressure is the dominant driving force for the reduction of ceria, the thermodynamic characteristics of surface and bulk oxygen are compared to elucidate the origin of dramatically enhanced surface Ce^{3+} concentration. At thermodynamic equilibrium, under given conditions, the chemical potentials (partial molar free energies) of oxygen in the surface and bulk regions are equal, despite the dramatically enhanced surface Ce^{3+} concentration. In contrast, the partial molar enthalpies and entropies are not required to be equal for the two regions, and the relative magnitudes of these properties provide essential insight. At equilibrium, the chemical potential of atomic oxygen is constant throughout the system and hence that in the solid state is equal to that in the gaseous state, giving:

$$\mu_O = \tfrac{1}{2}\mu_{O_2} = \tfrac{1}{2}\left(\mu^0_{O_2} + k_B T \ln p_{O_2}\right) \quad \textbf{(1)}$$

where $\mu^0_{O_2}$ is the standard potential at 1 atm, obtained from thermodynamic tables.[57] Because the extent of Ce reduction was measured directly, we are able to determine the equilibrium p_{O_2} (and hence the chemical potential) as a function of temperature at a constant (interpolated) $[Ce^{3+}]$ value. The results of the analysis are presented in Figure 7 for $[Ce^{3+}]_{bulk}$ = 0.0071 and for $[Ce^{3+}]_{surf}$ = 0.36, values falling within the experimentally observed ranges. The temperature where these specific concentrations have the same chemical potentials is ~ 521 °C. This is one of the measurement temperatures where the surface and bulk have the same equilibrium oxygen partial pressure for the selected Ce^{3+} concentrations.

The results in Figure 7 show that the bulk chemical potential varies linearly with temperature. Accordingly, the partial molar enthalpy (H_O) and entropy (S_O) can be readily derived by fitting to the relationship:

$$\mu_O = H_O - TS_O \quad \textbf{(2)}$$

The bulk thermodynamic parameters obtained, H_O^{bulk} = -3.9 eV and S_O^{bulk} = -0.90 meV K^{-1} for $[Ce^{3+}]_{bulk} = 0.0071$, are in excellent agreement with literature values.[49,58] Similar to the bulk free energy curve, the surface free energy curve is relatively linear with temperature, also shown in Figure 7. For $[Ce^{3+}]_{surf}$ = 0.36, we find $H_O^{surf} \approx$-2.9 ± 0.3 eV and $S_O^{surf} \approx$0.3 ± 0.3 meV K^{-1}, values that are elevated from bulk values by 1.0 eV and 1.2 meV K^{-1}, respectively. The surface thermodynamic quantities do not change appreciably even if we consider that a portion of the photoelectrons may originate from the oxidized bulk, despite the low effective attenuation length here (4 Å). Recently, DeCaluwe *et al.* estimated redox energetics from Ce^{3+} concentration data at a single oxygen activity by assuming that the surface and the bulk have the same defect interaction modes and energies, which is unlikely to be valid.[19] Our larger data set allows determining the energetics without assumptions.

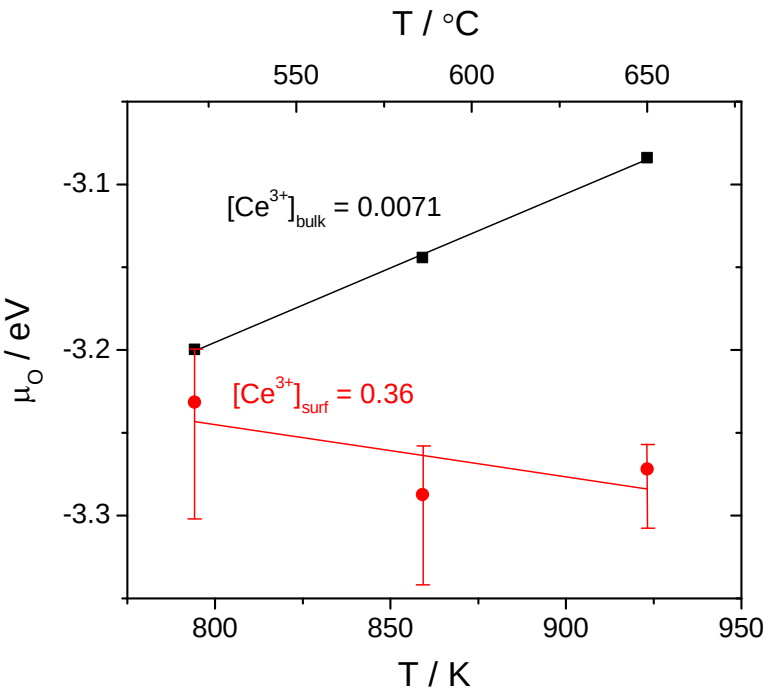

Figure 7. Chemical potential (partial molar free energy) of solid-state oxygen in the bulk and on the surface (for the oxidation states shown). Data points are from interpolations to power-law fits to the data in Figure 2. The chemical potential is not calculated at 466 °C because it cannot be obtained via a power-law interpolation for the selected SDC composition. Error bars in the surface chemical potential were obtained by propagating +/- 5 % uncertainty in $[Ce^{3+}]_{surf}$ (Figure 2) into Eq. (S3). Uncertainties in the absolute value of $[Ce^{3+}]_{surf}$ do not contribute significant error in the plot, and uncertainties in the bulk chemical potentials are smaller than the symbols. The standard enthalpy of O_2(g) is taken to be zero at 298.15 K and the standard entropy zero at 0 K.

The negative entropic contribution to the chemical potential of surface oxygen ($-TS_o$) compared to that of the bulk oxygen establishes that the preferential reduction of the surface becomes greater with decreasing temperature, behavior also evident directly from Figure 4. Therefore, the entropy-stabilized surface Ce^{3+} is expected to play a significant role in lower-temperature catalysis by increasing the availability of the localized electrons for catalytic reactions. We also anticipate that the reduced surfaces also have high oxygen vacancy concentration, though they were not measured directly. Further exploration of this point is the subject of future studies. In applications in which ceria is cycled between a reduced and an oxidized state (*e.g.*, between ~ CeO_2 and $CeO_{1.95}$ for solar thermochemical water-dissociation[59]), the results here confirms the reduced surface is stable and suggests the high Ce^{3+} concentration is one of the origins of the high reaction rate.

The partial molar entropy variation between the surface and the bulk oxygen is partially due to the different $[Ce^{3+}]$ at which the entropy values were determined. Moreover, the variation could be attributed to, among many phenomena, defect ordering, change in the vibrational characters, surface reconstruction, and site saturation. Possible short-range defect interaction modes include Ce^{3+}-Ce^{3+}, Ce^{3+}-dopant, Ce^{3+}-oxygen vacancy, *etc*. The tendency of surface defects to interact is large given the relatively large $[Ce^{3+}]_{surf}$ and surface dopant concentration values. Ordering not directly involving oxygen (*i.e.*, Ce^{3+}, oxygen vacancies and dopants) generally lead to an increase in the partial molar entropy of oxygen. Indeed, defect interactions have been observed experimentally with *ex situ* scanning tunneling microscopy.[21,60]

Long-range ordering can also play a role in stabilizing the surface Ce^{3+}. Because the surface structure of SDC (beyond symmetry and periodicity) is not known, we are not able to assess long-range ordering quantitatively. Nevertheless, the bulk phase diagrams of undoped and doped ceria have been investigated extensively[61,62] and may provide some insights to the surface mechanisms. In the absence of a dopant, nonstoichiometric ceria forms several bulk superstructures due to oxygen vacancy ordering in the composition range between CeO_2 and $CeO_{1.714}$ (< 640 °C).[61] However, the experimental phase diagram of 20 at.% Gd-doped ceria shows no long-range ordering for the same extent of oxygen deficiency, even at room temperature.[62] Dopants have been proposed to weaken the vacancy-vacancy interaction and suppress the formation of superstructures. Such mechanism is also likely operative on the surface, especially given the high surface Sm concentration. Moreover, the presence of two distinct cations will also modify the vibrational character of the cation-oxygen bond, and thus the vibrational partial molar entropy of oxygen. Further work on correlating surface oxygen chemical potential and dopant concentration is underway.

2.4 Conclusions

A quantitative picture of the equilibrium surface chemistry in Sm-doped CeO_2 is revealed using ambient-pressure X-ray photoelectron spectroscopy and electrochemical impedance spectroscopy. We show experimentally that the surface Ce^{3+} concentration is substantially enhanced from the bulk, especially at low bulk oxygen nonstoichiometries, and is only weakly dependent on temperature and oxygen activity. Thus, the surface of doped ceria remains highly reduced even under relatively oxidizing environments. Such behavior likely explains the origin of high surface activity in ceria as it is cycled between reduced and oxidized states. Analysis of the chemical potential of surface oxygen indicates a large deviation from the bulk values. Such a

difference has a significant entropic character, which plays a crucial role in stabilizing surface Ce^{3+}, particularly at lower temperatures.

3 QUASI IN-SITU STUDY OF PHASE TRANSFORMATION IN LITHIUM-ION BATTERIES

3.1 Introduction

Among the most intensely investigated materials for the positive electrodes of lithium-ion batteries is Li_xFePO_4 (LFP, with $0 \leq x \leq 1$). LFP undergoes a first-order phase transformation at well-defined compositions when lithium is added or removed, leading to lithium-rich and lithium-poor phases.[63] Understanding the lithium intercalation pathway in LFP is of crucial technological importance, as the intercalation kinetics directly determines the current density and efficiency of the electrode. In the past few years, significant progress has been made in understanding the LFP phase transformation, especially of single LFP particles.[64-70] A solid-solution pathway was also proposed based on first-principles[71] and phase-field modeling.[72,73] In this pathway, at a sufficiently large current, phase separation is suppressed in the nominally two-phase coexistence regime.

One of the most controversial topics surrounding lithium intercalation in LFP is the behavior under constant current conditions in a many-particle ensemble with a broad distribution of particle size, such as a realistic battery electrode. Experimentally, lithium intercalation and phase transformation in LFP ensembles have been studied using a wide range of techniques including *in-situ* X-ray and neutron diffraction[74-79] (typically averaging over the entire electrode), transmission electron microscopy[80-83] (typically sampling only a few particles), and electrochemical methods.[84,85] Micro-diffraction[86] at a resolution of several microns has also been employed. On one hand, some results suggest that LFP transformations proceed concurrently in almost all particles.[77,80] On the other hand, there are also evidences supporting the particle-by-particle intercalation pathway,[82] originally proposed for LFP by Delmas *et al*,[74] whereby only a small fraction of the particles undergoes phase transformation at any given time. Contrary to the "concurrent" intercalation pathway, two-phase coexistence occurs not at the single particle level but rather at the ensemble level. The electrode forms a "mosaic" of homogenous particles that are mostly either lithium-rich or lithium-poor.[67,68,73,74,87-89] The origin of the mosaic pathway remains unclear and has been attributed to minimization of the interfacial energy,[67] rapid phase boundary movement,[74] and fast inter-particle transport.[68,89] In the experimental work so far, the lack of spatial resolution or statistical relevance likely accounts for some of the discrepancies. The ability to image the local state-of-charge of a large number of particles that span the thickness of the electrode is needed to clarify the intercalation pathway in many-particle LFP electrodes.

In this work, we employed synchrotron-based scanning transmission X-ray microscopy (STXM) at the Advanced Light Source (beam line 5.3.2)[90] and transmission electron microscopy (TEM) to image the local state-of-charge and particle morphology, respectively, of a LFP electrode from a cycled coin-cell battery. We spanned the length scales of individual particles as well as the macroscopic electrode ensemble.

3.2 Experimental Methods

Standard coin battery cells consisting of ~ 35-µm-thick carbon-coated LFP/graphite composite cathode, Li anode, and 1.2 M $LiPF_6$/ethylene carbonate/ethyl methyl carbonate electrolyte were electrochemically cycled five times. A stable capacity of 150 mAh g^{-1} was obtained (Figure 8). To establish Fe L_3 reference absorption spectra of the limiting compositions $LiFePO_4$ and $FePO_4$, battery cells at 0 and 100 % state-of-charge were prepared by discharging and charging at 1/50 C, respectively. We then charged a battery to 75 mAh g^{-1} (50 % state-of-charge) at 1 C. Immediately upon reaching the target state-of-charge, we rapidly disassembled the cell inside a dry room and washed the electrode with an excess of dimethyl carbonate. This procedure was completed within ~ 4 min after terminating the charge, significantly faster than typical voltage relaxation times.[91,92] Because LFP particles are not in direct contact with one another in typical electrode microstructures (as shown recently by tomographic reconstruction[93]), further equilibration between LFP particles is unlikely after removing the electrolyte. We recognize, however, that lithium can re-distribute within each particle without external mass transport (*e.g.*, a solid-solution particle undergoes phase separation[71,73]). Finally, the composite electrode was mechanically cross-sectioned to yield a ~ 400-nm-thick sample.

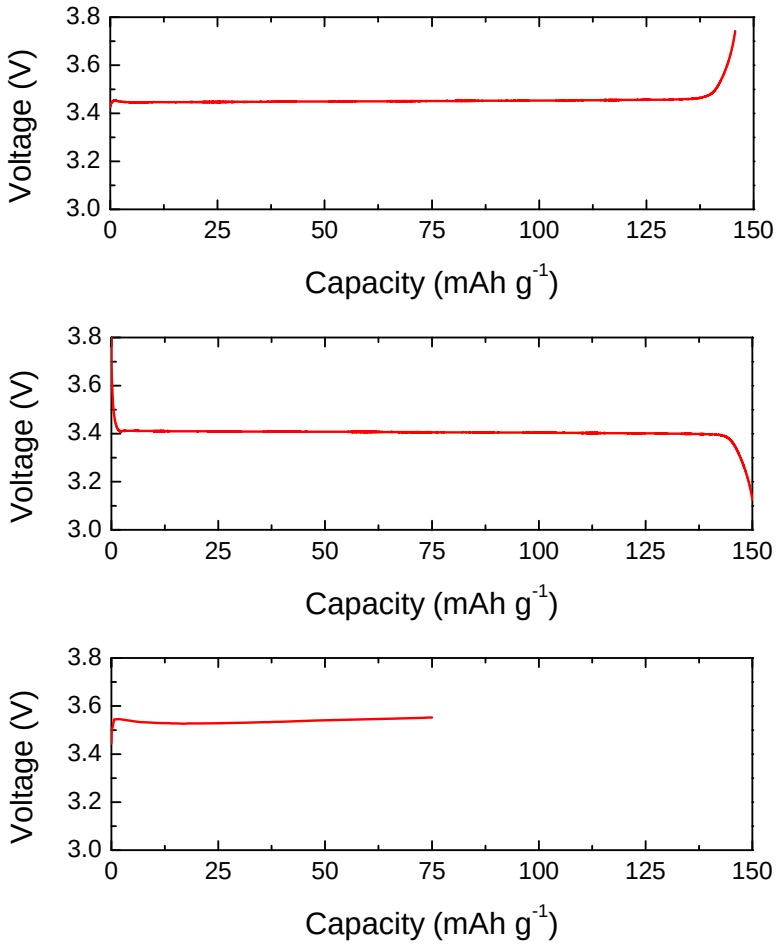

Figure 8: Voltage curves for **(top)** charging at 1/50 C to 100 % state-of-charge, **(middle)** discharging at 1/50 C to 0 % state-of-charge, and **(bottom)** charging at 1 C to 50 % state-of-charge.

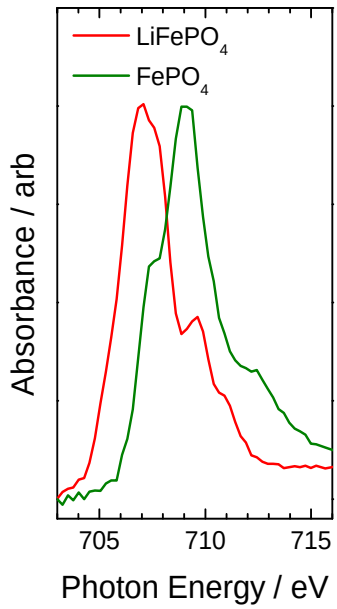

Figure 9. Fe L_3 X-ray absorption reference spectra taken from $LiFePO_4$ and $FePO_4$ electrodes lithiated and de-lithiated electrochemically.

Spatially resolved state-of-charge (Fe^{3+} molar fraction) maps were obtained by least-square fitting of STXM spectral images to a linear combination of the $FePO_4$ and $LiFePO_4$ reference spectra[94] using the Axis2000 software package[95]. In the reference samples, the absorption spectra showed negligible spatial variations. The reference spectra were obtained by averaging across several particles (Figure 9). Consistent with previous reports, a change in the Fe oxidation state (from 2+ to 3+) upon de-lithiation shifts the main absorption feature in the Fe L_3 edge from ~ 708 to ~ 710 eV.[96-100] Other previously reported spectral features were also satisfactorily reproduced. Excellent fits were obtained at all spatial positions, with a maximum residual of 0.8 % (averaged over all photon energies). An average state-of-charge was determined by ratioing the average thickness of $FePO_4$ and $LiFePO_4$ with appropriate material parameters. For the three regions analyzed, we obtained 49 % to 51 % average state-of-charge from the STXM maps (Figure 10). Not only is the state-of-charge independent of position along the thickness of the battery electrode, it is also essentially identical to the average, electrochemically determined state-of-charge. The excellent agreement between the state-of-charge determined electrochemically and *via* STXM validates our quantification strategy.

3.3 Results & Discussions

We measured the nanoscale state-of-charge for approximately 450 LFP particles in three 5 × 5 µm regions centered at approximately 26, 18, and 6 µm from the Al current collector, 5 × 5 µm regions centered at approximately 26, 18, and 6 µm from the Al current collector, respectively (Figure 10). In these maps, the hue shows the state-of-charge, with pure red

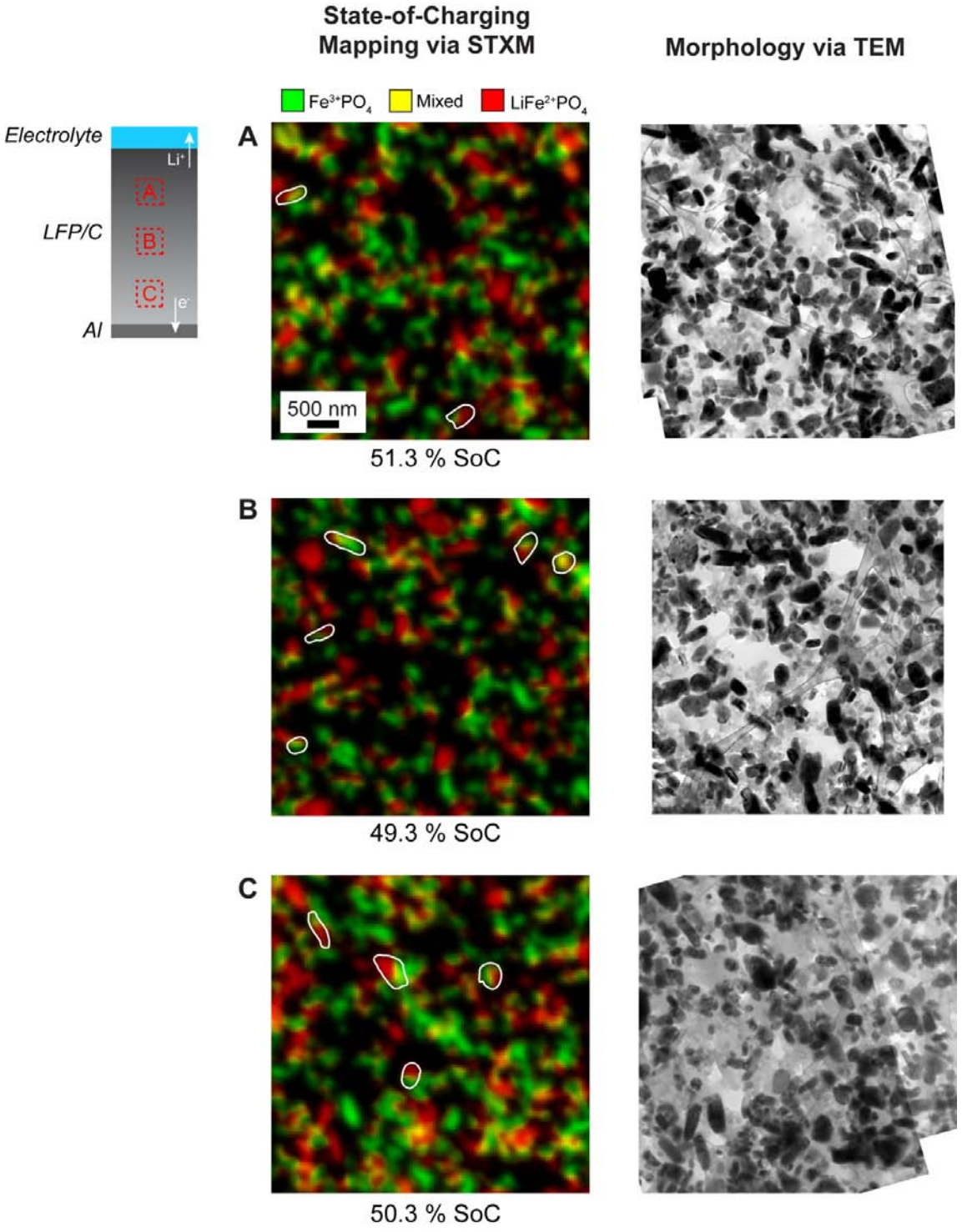

Figure 10. (Left) state-of-charge mapping obtained via scanning transmission X-ray microscopy and **(right)** morphology obtained via transmission electron microscopy of the same regions in the lithium iron phosphate composite electrode **(a)** 26 µm, **(b)** 18 µm **(c)** and 6 µm from the Al current collector. Hue and brightness give the local state-of-charge and lithium iron phosphate thickness, respectively. Outlined in white are particles in which two phases coexist within the same LFP particle; all other particles are single phase, either lithium-rich (red) or lithium

representing 0 %, (*i.e.*, $LiFePO_4$), yellow 50 %, and green 100 % (*i.e.*, $FePO_4$), whereas the brightness gives the relative thickness of the particles. A simple visual inspection of the STXM maps in Figure 10 reveals that there are significant inhomogeneities in the state-of-charge at the tens to hundreds of nm length scales, that is, adjacent particles have completely different states-of-charge. Notably, the extent of variation appears to be similar regardless of macroscopic position in the composite electrode, that is, close to the electrolyte (Figure 10a) or near the Al current collector (Figure 10c). The absence of a gradient in lithium content on the electrode and ion diffusion in the electrolyte is substantially faster than the charging time. In other words, there is no resistive loss to transport lithium from the surface of one particle to another.

Table 1. Statistics on the state-of-charge of lithium iron phosphate in a composite electrode, sampled either as a cross section or after dispersing the particles. Regions in cross-sectioned electrode are indicated in Figure 2.

	cross-sectioned electrode				dispersed electrode
	region A	region B	region C	total	
number of particles	142	167	144	453	81
fraction of lithium-poor particles	68 %	68 %	60 %	65 %	61 %
fraction of lithium-rich particles	31 %	29 %	37 %	32 %	36 %
fraction of mixed particles	1.4 %	3.0 %	2.8 %	2.4 %	3.7 %

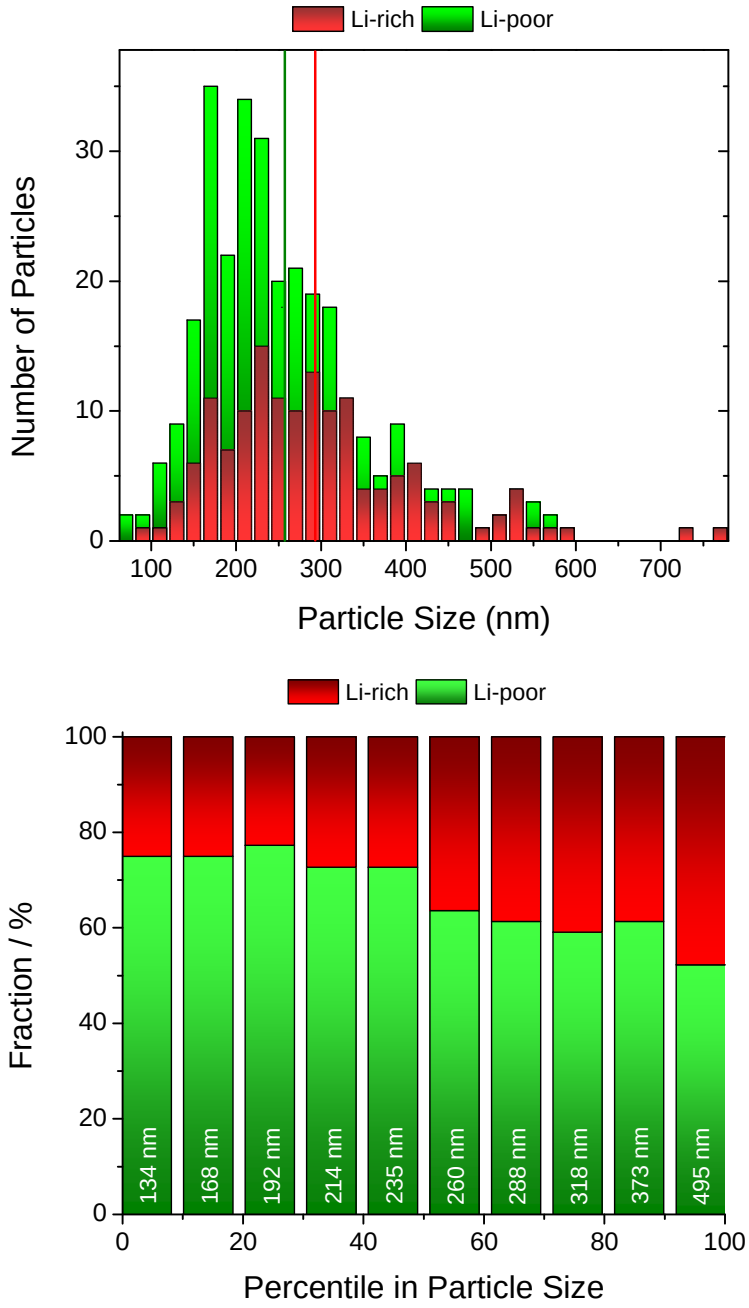

Figure 11. Particle-size distributions of all the single-phase particles shown in Figure 2. Vertical lines depict the average particle size. **(Top)** Number of particles vs. size. **(Bottom)** The fraction of de-lithiated particles plotted as a function of percentile of particle size (in increments of 10 %). Average particle size in each percentile range also shown. Each bar consists of 44 particles.

Having established the absence of a macroscopic diffusion front within the LFP electrode, we

now turn to the nanoscale variation in the state-of-charge. At first glance, the particles appear to exhibit state-of-charge ranging from 0 to 100 %. However, because the two-dimensional STXM measurement averages through the thickness of the cross section, the charge state of overlapped particle are averaged in the maps. To resolve this ambiguity, we identified overlapping particles by imaging the same regions with TEM. Combined TEM imaging (Figure 10, right column) and STXM state-of-charge mapping (Figure 10, left column) reveals that almost all scan locations that indicate an intermediate state-of-charge (yellow in Figure 10) are in fact overlapped particles. As summarized in Table 1, of the approximately 450 LFP particles examined, 65 % of the particles are lithium-poor (green hue; defined as $Li_{\alpha}FePO_4$, with $\alpha \leq 0.15$) meaning that they have already transformed and are nearly charged. On the other hand, 32 % are lithium-rich (red hue; defined as $Li_{\beta}FePO_4$, with $\beta \geq 0.85$), that is, they remain untransformed and are nearly discharged. Only 11 particles (2 %) exhibit intermediate states-of-charge (outlined in white in Figure 10). All of these particles contain phase boundaries separating lithium-rich and lithium-poor regions. These particles were undergoing transformations when the charging was terminated. So the time needed to transform these few particles is ~ 50 times smaller than the time needed to charge the entire battery electrode. Even without further analysis, our results directly show that the transformation kinetics proceed rapidly once they are initiated, as suggested by previous experimental results.[74]

We also performed image analysis on the STXM maps and TEM images to correlate the state-of-charge to LFP particle dimensions. Since most particles are ellipsoidal, we carried out the size distribution analysis using the square root of the particle area, and the longest and shortest line that goes through the particle's center of gravity (essentially length of the long and short axes, respectively). All measures of particle size gave similar correlation between state-of-charge and size. For simplicity, we present the state-of-charge distribution as a function of the length of the long axis. The size distributions of lithium-rich and lithium-poor LFP particles (Figure 11, top) show some differences. The average particle size (length of the long axis) is 256 nm for lithium-poor LFP and 294 nm for lithium-rich particles. The difference in the averaged particle size resolves the apparent discrepancy that 65 % of the particles are de-lithiated for our half-charged electrode. At first, the difference in the average size seems to suggest that smaller particles are de-lithiated preferentially. However, upon a closer investigation of the size distribution of the two phases, we find that a substantial number of small and large particles still remain lithiated and de-lithiated, respectively. Figure 11, bottom, shows the fraction of lithium-rich and lithium-poor LFP particles as a function of the percentile in particle size (plotted in increments of 10 %). For our half-charged electrode, 25 % of the smallest particles (with an average size of 134 nm), remain lithiated. Similarly, 53 % of the largest particles (with an average size of 495 nm) are de-lithiated. Thus, the probability of finding a particular LFP particle in either lithiation state depends only weakly on its size.

Since a macroscopic diffusion front was absent in our LFP electrode, we further improved the confidence of our analysis by imaging particles with reduced overlap prepared by dispersing the electrode. LFP powder scraped from the same electrode was suspended and sonicated in

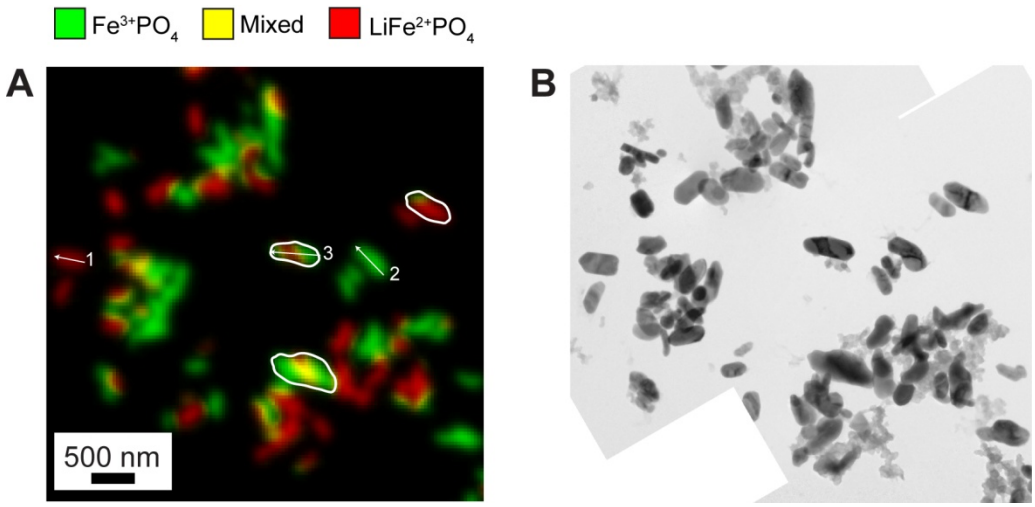

Figure 12. (a) State-of-charge mapping and **(b)** morphology of lithium iron phosphate electrode powder dispersed by sonication. From the same electrode shown in Figure 2. Outlined in white are particles in which two phases coexist within the same particle.

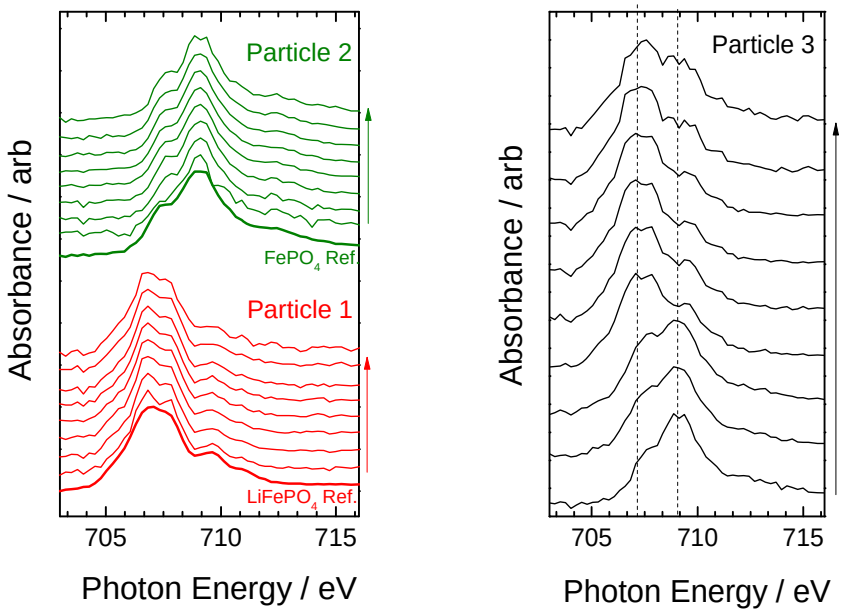

Figure 13. X-ray absorption line scans of select lithium iron phosphate particles indicated in Figure 4. Particles 1 and 2 are single phase and the X-ray absorption spectra showed negligible variations within the particle. Particle 3 contains two phases, separated by a well-defined boundary. Reference spectra (heavy lines) of the limiting compositions are also shown for comparison.

anhydrous ethanol, which was then pipetted onto a thin Si_3N_4 membrane. The STXM map and TEM image, Figure 12, show considerably better inter-particle isolation than those of the cross-sectioned electrode. All of the experimental features discussed above were reproduced with the dispersed powder sample: (1) strong heterogeneity in the local state-of-charge, (2) 61 % of the particles are lithium-rich and 36 % are lithium-poor, and (3) only 3 out of the 81 particles are undergoing transformation. X-ray absorption line scans across a lithium-poor, a lithium-rich, and a two-phase particle are shown in Figure 12.

Summarizing our experimental results, we directly observed that lithium-rich and lithium-poor LFP particles dominated the electrode, and only ~ 2 % of the particles were undergoing de-lithiation. These observations establish unambiguously that the mosaic pathway is the prevailing many-particle intercalation route under the conditions examined. Furthermore, contrary to the common expectation that smaller particles would transform before larger ones, we observed only a weak correlation between the state-of-charge and the particle size. Next, we use these quantitative observations to elucidate the physical origin of the mosaic configuration and to give insights to the processes that limit transformation in many-particle LFP electrodes.

When a stable phase boundary forms upon de-intercalation, its lithium chemical potential is at a value higher than that of the electrolyte. This overpotential constitutes the driving force of the phase transformation, that is, for moving the phase boundary. While forming the phase boundary perturbs the lithium chemical potential of the electrolyte and single-phase particles,[68,89] the perturbation is vanishingly small for a real battery electrode with fast inter-particle transport, such as ours. That is, the electrolyte and/or particles in the electrode act as reservoirs that can rapidly sink (or source) lithium. We next consider two phenomena that can plausibly limit the rate of phase transformation in LFP: (1) the initiation of phase transformation (*e.g.*, a nucleation-like event), and (2) the propagation of the phase boundary (*i.e.*, the growth of a lithium-poor phase within the particle during de-intercalation).

If the energetic barrier of a nucleation-like event is large compared to that of boundary propagation, the supersaturation needed to achieve the required nucleation rate sets the electrode overpotential. This overpotential also readily propagates the phase boundary. At a given overpotential, the time needed to complete a particle's transformation is small compared to the average time needed to initiate nucleation. Thus, we expect the number of particles undergoing transformation to be much smaller than the total number of particles, which is precisely what we observe in the LFP electrode. In this limit the charging current is equal to the nucleation rate times the average particle charge, and the overpotential required to attain a particular charging rate is determined by the nucleation rate, not by the phase-boundary velocity.

Our observations are inconsistent with the other limiting regime, where propagation of the phase boundary (controlled by, for example, lithium diffusion or surface reaction) sets the overpotential. In this limit, the overpotential that gives significant nucleation rates is insufficient to sweep a boundary through a particle before nucleation events occur in other particles. Then, most particles should transform at the same time, unless the boundary motion has a strong dependence on size. But we have found no such dependence. Our statistics, with ~2 % particles transforming at once, show that our LFP electrode is far from being in this regime.

Additionally, our observations also suggest that charging in LFP could not have proceeded via the solid-solution pathway, where phase separation is suppressed entirely. Similar to the two-phase transformation pathway limited by boundary propagation, LFP particles a solid-solution pathway would start charging concurrently. For a half-charged electrode with no electrolyte

transport limitations, we would expect to see a significant fraction of the particles in an intermediate state-of-charge. This was not observed, at least under a 1 C charging rate.

Having established that charging in LFP is limited by the initiation of phase transformation, we now turn to the particle size distribution of the lithium-rich and lithium-poor phases. The size distributions of particles that have yet to transform and those that have already transformed give us insights into the probability of initiating phase transformation as a function of particle size. In the nucleation-limited regime, we expect that the nucleation probability to correlate monotonically with the surface area of the particles (for heterogeneous nucleation), provided that the barrier height is independent of particle size and morphology. However, this was not observed in our experiment. Our results likely indicate a non-trivial (and possibly non-monotonic) dependence of nucleation barrier height on the particle size (and maybe also on morphology). One possibility is that the extent and nature of carbon-coating depends on particle size and morphology, which subsequently leads to significant variations between particles. Detailed correlation of particle surface characteristics and the sequence of transformation is underway.

3.4 Conclusion

We have combined the high chemical and spatial resolutions of STXM and TEM, respectively, to map the state-of-charge in individual LFP particles over the entire thickness of a battery electrode. The average lithium content of the particles did not vary with distance from the current collector, establishing that Li transport through the electrolyte is relatively fast under a 1 C charging current. When the entire electrode was charged to 50 %, almost all the LFP particles are nearly completely charged or discharged, in other words, the mosaic limit of a transforming particle ensemble. Furthermore, only a small fraction of the particles (~ 2 %), those with both lithium-rich and lithium-poor regions, are undergoing phase transformation at one time. Therefore, the time needed to charge individual LFP particles completely is much shorter (about 50 times) than the time needed to charge the entire particle ensemble. These observations establish that the rate of initiating the phase transformation in a particle is much slower than the rate of completing the phase transformation. Furthermore, the sequence of de-lithiation depends only weakly on the particle size, and, subsequently, on the particle's surface area. This finding suggests that the barrier height for nucleation-like events scale with particle size in a non-linear and possibly non-monotonic manner. This work provides direct guidance for how to improve the performance of LFP battery electrodes, namely, by increasing the rate of the nucleation-like events.

4 CONCLUSIONS

We have successfully developed and employed synchrotron-based X-ray spectroscopy and microscopy to study electrochemical phenomena in electrocatalysts for fuel cells and electrolyzers, and in phase-transforming materials for batteries.

Using ceria-based electrocatalyst as a model system, we employed ambient pressure X-ray photoelectron spectroscopy to study defect thermodynamics on the first few atomic layers of the surface exposed to the gas phase. We observed that the surface defect concentrations, particularly of the localized electrons, differ sharply from that of the bulk. Comparison of the surface to the bulk thermodynamics revealed a significant difference, both in terms of the defect formation enthalpy and the formation entropy. We hypothesized that ease of formation of localized electronic defects on the surface relative to the bulk of ceria may be partly responsible for the high activity for hydrogen oxidation in fuel cells and for water-splitting in electrolyzers and thermochemical cycles.

Turning to batteries, we have successfully carried out quasi-in-situ X-ray microscopy to study phase transformation in lithium iron phosphate positive electrodes, That is, we first charged or discharged the battery to a given states under constant current conditions, rapidly removed the liquid electrolyte to freeze lithium exchange between particles, and then examined them using the X-ray microscope. We spanned the length scales of individual particles as well as the macroscopic electrode ensemble. We imaged approximately 450 individual LFP particles across the thickness of the electrode. We show unambiguously that phase transformation proceeds via the particle-by-particle pathway, rather than via the concurrent pathway as proposed by previous work. In fact, the fraction of particles that are actively undergoing phase transformation (at 50 % state-of-charge) is remarkably small, only ~ 2 %. A statistical analysis revealed a weak correlation between state-of-charge and particle size, indicating that there is little preference to de-lithiate small or large particles selectively.

REFERENCES

1 Lewis, N. S. & Nocera, D. G. Powering the planet: Chemical challenges in solar energy utilization. *Proc. Nat. Acad. Sci. U.S.A.* **103**, 15729-15735 (2006).

2 Trovarelli, A. Catalytic properties of ceria and CeO2-containing materials. *Cat. Rev. - Sci. Eng.* **38**, 439-520 (1996).

3 Atkinson, A. *et al.* Advanced anodes for high-temperature fuel cells. *Nature Mat.* **3**, 17-27 (2004).

4 Mogensen, M., Sammes, N. M. & Tompsett, G. A. Physical, chemical and electrochemical properties of pure an doped ceria. *Solid State Ionics* **129**, 63-94 (2000).

5 Murray, E. P., Tsai, T. & Barnett, S. A. A direct-methane fuel cell with a ceria-based anode. *Nature* **400**, 649-651 (1999).

6 Park, S., Vohs, J. M. & Gorte, R. J. Direct oxidation of hydrocarbons in solid-oxide fuel cell. *Nature* **404**, 265-267 (2000).

7 Park, J. B. *et al.* High catalytic activity of Au/CeOx/TiO2(110) controlled by the nature of the mixed-metal oxide at the nanometer level. *Proc. Natl. Acad. Sci.* **163**, 4975-4980 (2009).

8 Rodriguez, J. A. *et al.* Activity of CeOx and TiOx nanoparticles grown on Au(111) in the water-gas-shift reaction. *Science* **318**, 1757-1760 (2007).

9 Ganduglia-Pirovano, M. V., Da Silva, J. L. F. & Sauer, J. Density-Functional Calculations of the Structure of Near-Surface Oxygen Vacancies and Electron Localization on CeO2ð111Þ. *Phys. Rev. Lett.* **102**, 026101 (2009).

10 Li, H.-Y. *et al.* Multiple configurations of the two excess 4f electrons on defective CeO2(111): Origin and implications. *Phys. Rev. B* **79**, 193401 (2009).

11 Lai, W. & Haile, S. M. Impedance Spectroscopy as a Tool for chemical and Electrochemical Analysis of Mixed Conductors: A Case Study of Ceria. *J. Am. Ceram. Soc.* **88**, 2979-2997 (2005).

12 Lu, C., Worrell, W. L., Vohs, J. M. & Gorte, R. J. A comparison of Cu-ceria-SDC and Au-ceria-SDC composites for SOFC anodes. *J. Electrochem. Soc.* **150**, A1357-A1359 (2003).

13 Zhang, C. J. *et al.* Measuring fundamental properties in operating solid oxide electrochemical cells by using in situ X-ray photoelectron spectroscopy. *Nature Mat.* **9**, 944-949 (2010).

14 Adler, S. Factors Governing Oxygen Reduction in Solid Oxide Fuel Cell Cathodes. *Chem. Rev.* **104**, 4791-4844 (2004).

15 Chueh, W. C., Yong, H., Jung, W. & Haile, S. M. High Electrochemical Activity of the Oxide Phase in Pt-Ceria & Ni-Ceria Composite Anode. *Nature Mater.* **11**, 155-161 (2012).

16 Murugan, B. & Ramaswamy, A. V. Defect-Site Promoted Surface Reorganization in Nanocrystalline Ceria for the Low-Temperature Activation of Ethylbenzene. *J. Am. Chem. Soc.* **129**, 3062-3063 (2007).

17 Nolan, M., Parker, S. & Watson, G. W. CeO2 catalysed conversion of CO, NO2 and NO from first principles energetics. *Phys. Chem. Chem. Phys.* **8**, 216-218 (2005).

18 Sayle, T. X. T., Parker, S. C. & Catlow, C. R. A. The role of oxygen vacancies on ceria surfaces in the oxidation of carbon monoxide. *Surf. Sci.* **316**, 329-336 (1994).

19 DeCaluwe, S. C. *et al.* In Situ Characterization of Ceria Oxidation States in High-Temperature Electrochemical Cells with Ambient Pressure XPS. *J. Phys. Chem. C* **114**, 19853-19861 (2010).
20 Gao, P. *et al.* Electrically Driven Redox Process in Cerium Oxides. *J. Am. Chem. Soc.* **132**, 4197-4201 (2010).
21 Esch, F. *et al. Science* **309**, 752 (2005).
22 Henderson, M. A., Perkins, C. L., Engelhard, M. H., Thevuthasan, S. & Peden, C. H. F. Redox properties of water on the oxidized and reduced surfaces of CeO2(111). *Surf. Sci.* **526**, 1-18 (2003).
23 Liu, X., Zhou, K., Wang, L., Wang, B. & Li, Y. Oxygen Vacancy Clusters Promoting Reducibility and Activity of Ceria Nanorods. *J. Am. Chem. Soc.* **131**, 3140-3141 (2009).
24 Mullins, D. R., Overbury, S. H. & Huntley, D. R. Electron spectroscopy of single crystal and polycrystalline cerium oxide surfaces. *Surf. Sci.* **409**, 307-319 (1998).
25 Mullins, D. R., Radulovic, P. V. & Overbury, S. H. Ordered cerium oxide thin films grown on Ru(0001) and Ni(111). *Surf. Sci.* **429**, 186-198 (1999).
26 Shyu, J. Z. *et al.* Characterization of Pdly-Alumina Catalysts Containing Ceria. *J. Catal.* **114**, 23-33 (1988).
27 Tschope, A. Interface Defect Chemistry and Effective Conductivity in Polycrystalline Cerium Oxide. *J. Electroceramics* **14**, 5-23 (2005).
28 Bishop, S. R., Duncan, K. L. & Wachsman, E. D. Surface and bulk oxygen non-stoichiometry and bulk chemical expansion in gadolinium-doped cerium oxide. *Acta Mater.* **57**, 3596-3605 (2009).
29 Chen, S. S. *et al.* Direct calorimetric measurement of grain boundary and surface enthalpies in yttria-stabilized zirconia. *Phys. Chem. Chem. Phys.* **11**, 3039-3042 (2009).
30 Zhou, G., Shah, P. R., Montini, T., Fornasiero, P. & Gorte, R. J. Oxidation enthalpies for reduction of ceria surfaces. *Surf. Sci.* **601**, 2512-2519 (2007).
31 Lee, Y. *et al.* Raman Analysis of Mode Softening in Nanoparticle CeO2−δ and Au-CeO2−δ during CO Oxidation. *J. Am. Chem. Soc.* **133**, 12952-12955 (2011).
32 Yang, Z., Woo, T. K., Baudin, M. & Hermansson, K. Atomic and electronic structure of unreduced and reduced CeO2 surfaces: A first-principles study. *J. Chem. Phys.* **120**, 7741-7749 (2004).
33 Jiang, Y., Adams, J. B. & van Schilgaarde, M. Density-functional calculation of CeO2 surfaces and prediction of effects of oxygen partial pressure and temperature on stabilities. *J. Chem. Phys.* **123**, 064701 (2005).
34 Conesa, J. C. Computer modeling of surfaces and defects on cerium dioxide. *Surf. Sci.* **339**, 337-352 (1995).
35 Chen, H.-T., Choi, Y. M., Liu, M. & Lin, M. C. A Theoretical Study of Surface Reduction Mechanisms of CeO2(111) and (110) by H2. *ChemPhysChem* **8**, 849-855 (2007).
36 Ganduglia-Pirovano, M. V., Hofmann, A. & Sauer, J. Oxygen vacancies in transition metal and rare earth oxides: Current state of understanding and remaining challenges. *Surf. Sci. Rep.* **62**, 219-279 (2007).
37 Fabris, S., Vicario, G., Balducci, G., de Gironcoli, S. & Baroni, S. Electronic and Atomistic Structures of Clean and Reduced Ceria Surfaces. *J. Phys. Chem. B* **2005**, 22860-22847 (2005).

38 Herschend, B., Baudin, M. & K., H. Oxygen vacancy formation for transient structures on the CeO2(110) surface at 300 and 750 K. *J. Chem. Phys.* **126**, 234706 (2007).
39 Nolan, M., Grigoleit, S., Salye, D. C., C., P. S. & Watson, G. W. Density functional theory studies of the structure and electronic structure of pure and defective low index surfaces of ceria. *Surf. Sci.* **576**, 217-229 (2005).
40 Badwal, S. P. S. *et al.* Application of work function measurements for surface monitoring of oxide electrode materials (La,Sr)(Co,Mn,Fe)O3. *J. Phys. Chem. Solids* (2001).
41 De Souza, R. A. A universal empirical expression for the isotope surface exchange coefficients (k*) of acceptor-doped perovskite and fluorite oxides. *Phys. Chem. Chem. Phys.* **8**, 890-897 (2006).
42 Bluhm, H. *et al.* Soft X-ray microscopy and spectroscopy at the molecular environmental science beamline at the Advanced Light Source. *J. Electron. Spectrosc.* **150**, 86-104 (2006).
43 Grass, M. E. *et al.* New ambient pressure photoemission endstation at Advanced Light Source beamline 9.3.2. *Rev. Sci. Instrum.* **81**, 053106 (2010).
44 Pfau, A. & D., S. K. The electronic structure of stoichiometric and reduced CeO, surfaces: an XPS, UPS and HREELS study. *Surf. Sci.* **321**, 71-80 (1994).
45 Burroughs, P., Hamnett, A., Orchard, A. F. & Thornton, G. Satellite Structure in theX-Ray Photoelectron Spectra of some Binary and Mixed Oxides of Lanthanum and Cerium. *J. C. S. Dalton*, 1686-1698 (1976).
46 Holgado, J. P., Alvarez, R. & Munuera, G. Study of CeO2 XPS spectra by factor analysis: reduction of CeO2. *Appl. Surf. Sci.* **161**, 301-315 (2000).
47 Romeo, M., Bak, K., El Fallah, J., Le Normand, F. & Hilaire, L. XPS Study of the Reduction of Cerium Dioxide. *Surf. Interface. Anal.* **20**, 508-512 (1993).
48 Whaley, J. A. *et al.* Note: Fixture for characterizing electrochemical devices in-operandoin traditional vacuum systems. *Rev. Sci. Instrum.* **81**, 086104 (2010).
49 Chueh, W. C. & Haile, S. M. Electrochemical studies of capacitance in cerium oxide thin films and its relationship to anionic and electronic defect densities. *Phys. Chem. Phys. Chem.* **11**, 8144-8148 (2009).
50 Jamnik, J. & Maier, J. Generalised equivalent circuits for mass and charge transport: chemical capacitance and its implications. *Phys. Chem. Chem. Phys.* **3**, 1668-1678 (2001).
51 Avila-Paredes, H. J., Choi, K., Chen, C.-T. & Kim, S. Dopant-concentration dependence of grain-boundary conductivity in ceria: A space-charge analysis. *J. Mater. Chem.* **19**, 4837-4842 (2009).
52 Kim, S. & Maier, J. On the Conductivity Mechanism of Nanocrystalline Ceria. *J. Electrochem. Soc.* **149**, J73-J83 (2002).
53 Maier, J. *Physical Chemistry of Ionic Materials*. (Wiley, 2004).
54 W. F. Egelhoff, J. Core-Level Binding-Energy shifts at Surfaces and in Solids. *Surf. Sci. Rep.* **6**, 253-415 (1987).
55 Ketteler, G. *et al.* The Nature of Water Nucleation Sites on TiO2(110) Surfaces Revealed by Ambient Pressure X-ray Photoelectron Spectroscopy. *J. Phys. Chem. C* **111**, 8728-8282 (2007).
56 Chueh, W. C., Yang, C.-K., Garland, C. M., Lai, W. & Haile, S. M. Unusual Decrease in Conductivity Upon Hydration in Acceptor Doped, Microcrystalline Ceria. *Phys. Chem. Chem. Phys.* **13**, 6442-6451 (2011).

57 Barin, I. *Therrnochernical Data of Pure Substances*. (VCH, 1995).
58 Kobayashi, T., Wang, S., Dokiya, M., Tagawa, H. & Hashimoto, T. Oxygen nonstoichiometry of Ce1-ySmyO2-0.5y-x (y=0.1, 0.2). *Solid State Ionics* **126**, 349-357 (1999).
59 Chueh, W. C. *et al.* High-Flux Solar-Driven Thermochemical Dissociation of CO2 and H2O Using Nonstoichiometric Ceria. *Science* **330**, 1797-1801 (2010).
60 Torbrugge, S. & Reichling, M. Evidence of Subsurface Oxygen Vacancy Ordering on CeO2(1110. *Phys. Rev. Lett.* **99**, 056101 (2007).
61 Riess, I., Ricken, M. & Nolting, J. On the Specific Heat of Nonstoichiometric Ceria. *J. Solid State Chem.* **57**, 314-312 (1985).
62 Stelzer, N., Nolting, J. & Riess, I. Phase Diagram of Nonstoichiometric 10 mol% Gd2O3-Doped Cerium Oxide Determined from Specific Heat Measurements. *J. Solid State Chem.* **117**, 392-397 (1995).
63 Padhi, A. K., Nanjundaswamy, K. S. & Goodenough, J. B. Phospho-olivines as positive-electrode materials for rechargeable lithium batteries. *J. Electrochem. Soc.* **144**, 1188-1194 (1997).
64 Han, B. C., Ven, A. V. d., Morgan, D. & Ceder, G. Electrochemical modeling of intercalation processes with phase field models. *Electrochim. Acta* **49**, 4691-4699 (2004).
65 Singh, G. K., Ceder, G. & Bazant, M. Z. Intercalation dynamics in rechargeable battery materials: General theory and phase-transformation waves in LiFePO4. *Electrochim. Acta* **53**, 7599-7613 (2008).
66 Burch, D. & Bazant, M. Z. Size-Dependent Spinodal and Miscibility Gaps for Intercalation in Nanoparticles. *Nano Lett.* **9**, 3795-3800 (2009).
67 Van der Ven, A., Garikipati, K., Kim, S. & Wagemaker, M. The Role of Coherency Strains on Phase Stability in LixFePO4: Needle Crystallites Minimize Coherency Strain and Overpotential. *J. Electrochem. Soc.* **11**, A949-A957 (2009).
68 Dreyer, W. *et al.* The thermodynamic origin of hysteresis in insertion batteries. *Nat. Mater.* **9**, 448-453 (2010).
69 Lai, W. Electrochemical modeling of single particle intercalation battery materials with different thermodynamics. *J. Power Sources* **196**, 6534-6553 (2010).
70 Safari, M. & Delacourt, C. Mathematical Modeling of Lithium Iron Phosphate Electrode: Galvanostatic Charge/Discharge and Path Dependence. *J. Electrochem. Soc.* **158**, A63-A73 (2011).
71 Malik, R., Zhou, F. & Ceder, G. Kinetics of non-equilibrium lithium incorporation in LiFePO4. *Nat. Mater.* **10**, 587-590 (2011).
72 Bai, P., Cogswell, D. A. & Bazant, M. Z. Suppression of Phase Separation in LiFePO4 Nanoparticles During Battery Discharge. *Nano Lett.* **11**, 4890-4896 (2011).
73 Cogswell, D. A. & Bazant, M. Z. Coherency Strain and the Kinetics of Phase Separation in LiFePO4 Nanoparticles. *ACS Nano* **6**, 2215-2225 (2012).
74 Delmas, C., Maccario, M., Croguennec, L., Cras, F. L. & Weill, F. Lithium deintercalation in LiFePO4 nanoparticles via a domino-cascade model. *Nat. Mater.* **7**, 665-671 (2008).
75 Meethong, N. *et al.* Electrochemically Induced Phase Transformation in Nanoscale Olivines Li1-xMPO4 (M) Fe, Mn). *Chem. Mater.* **20**, 6189-6198 (2008).
76 Kao, Y.-H. *et al.* Overpotential-Dependent Phase Transformation Pathways in Lithium Iron Phosphate Battery Electrodes. *Chem. Mater.* **22**, 5845-5855 (2010).

77 Badi, S.-P. *et al.* Direct synthesis of nanocrystalline Li0.90FePO4: observation of phase segregation of anti-site defects on delithiation. *J. Mater. Chem.* **21**, 10085-10093 (2011).
78 Sharma, N. *et al.* Direct Evidence of Concurrent Solid-Solution and Two-Phase Reactions and the Nonequilibrium Structural Evolution of LiFePO4. *J. Am. Chem. Soc.* **134**, 7867-7873 (2012).
79 Gibot, P. *et al.* Room-temperature single-phase Li insertion/extraction in nanoscale LixFePO4. *Nat. Mater.* **7**, 741-747 (2008).
80 Laffont, L. *et al.* Study of the LiFePO4/FePO4 Two-Phase System by High-Resolution Electron Energy Loss Spectroscopy. *Chem. Mater.* **2006**, 5520-5529 (2006).
81 Chen, G., Song, X. & Richardson, T. J. Electron Microscopy Study of the LiFePO4 to FePO4 Phase Transition. *Electrochem. Solid St.* **9**, A295-A298 (2006).
82 Brunetti, G. *et al.* Confirmation of the Domino-Cascade Model by LiFePO4/FePO4 Precession Electron Diffraction. *Chem. Mater.* **23**, 4515-4524 (2011).
83 Gu, L. *et al.* Direct Observation of Lithium Staging in Partially Delithiated LiFePO4 at Atomic Resolution. *J. Am. Chem. Soc.* **133**, 4661-4663 (2011).
84 Allen, J. L., Low, T. R. & Wolfenstine, J. Kinetic Study of the Electrochemical FePO4 to LiFePO4 Phase Transition. *Chem. Mater.* **19**, 2108-2111 (2007).
85 Oyama, G., Yamada, Y., Natsui, Y., Nishimura, S. & Yamada, A. Kinetics of Nucleation and Growth in Two-Phase Electrochemical Reaction of LixFePO4. *J. Phys. Chem. C* **116**, 7306-7311 (2012).
86 Liu, J., Kunz, M., Chen, K., Tamura, N. & Richardson, T. J. Visualization of Charge Distribution in a Lithium Battery Electrode. *J. Phys. Chem. Lett.* **1**, 2120-2123 (2010).
87 Wagemaker, M., Borghols, W. J. H. & Mulder, F. M. Large impact of particle size on insertion reaction. A case for anatase LixTiO2. *J. Am. Chem. Soc.* **129**, 4323-4327 (2007).
88 Wagemaker, M., Mulder, F. M. & Van der Ven, A. The Role of Surface and Interface Energy on Phase Stability of Nanosized Insertion Compounds. *Adv. Mater.* **21**, 2703-2709 (2009).
89 Burch, D. *Intercalation Dynamics in Li-ion Batteries* Ph.D thesis, Massachusetts Institute of Technology, (2009).
90 Kilcoyne, A. L. D. *et al.* Interferometer-controlled scanning transmission X-ray microscopes at the Advanced Light Source. *J. Synchrotron Rad.* **10**, 125-136 (2003).
91 Park, S., Kameyama, K. & Yao, T. Relaxation Crystal Analysis of LiFePO4 Cathode for Li-Ion Secondary Battery. *Electrochem. Solid St.* **15**, A49-A52 (201).
92 Lee, K. T., Kan, W. H. & Nazar, L. F. Proof of Intercrystallite Ionic Transport in LiMPO4 Electrodes (M) Fe, Mn). *J. Am. Chem. Soc.* **131**, 6044-6045 (2009).
93 Ender, M., Joos, J., Carraro, T. & Ivers-Tiffee, E. Three-dimensional reconstruction of a composite cathode for lithium-ion cells. *Electrochem. Comm.* **13**, 166-168 (2011).
94 Liu, X. *et al.* Phase Transformation and Lithiation Effect on Electronic Structure of LixFePO4: An In-Depth Study by Soft X-ray and Simulations. *J. Am. Chem. Soc.*, In Press. (2012).
95 *http://unicorn.mcmaster.ca/aXis2000.html*.
96 Augustsson, A. *et al.* Electronic structure of phospho-olivines LixFePO4 (x=0,1) from soft-x-ray-absorption and -emission spectroscopies. *J. Chem. Phys.* **123**, 184717 (2005).

97 Hunt, A., Ching, W.-Y., Chiang, Y.-M. & Moewes, A. Electronic structures of LiFePO4 and FePO4 studied using resonant inelastic x-ray scattering. *Phys. Rev. B* **73**, 205120 (2006).
98 Kurosumi, S. *et al.* Resonant Photoemission Spectroscopy of the Cathode Material LixFePO4 for Lithium Ion Battery. *J. Phys. Chem. C* **115**, 25519-25522 (2011).
99 Wang, X.-J. *et al.* Investigation of the structural changes in Li1-xFePO4 upon charging by synchrotron radiation techniques. *J. Mater. Chem.* **21**, 11406-11411 (2011).
100 Yang, S. *et al.* Soft X-ray XANES studies of various phases related to LiFePO4 based cathode materials. *Energy Environ. Sci.* **5**, 7007-7016 (2012).

DISTRIBUTION

1	MS0899	Technical Library	9536 (electronic copy)
1	MS0359	D. Chavez, LDRD Office	1911


Sandia National Laboratories